



INFILTRATION-INHIBITING REACTION OF GADOLINIUM ZIRCONATE THERMAL BARRIER COATINGS WITH CMAS MELTS[†]

Stephan Krämer,^{§,*} James Yang, Carlos G. Levi^{*}

Materials Department, University of California, Santa Barbara, CA 93106-5050, USA

Abstract

The thermochemical interaction between a $\text{Gd}_2\text{Zr}_2\text{O}_7$ thermal barrier coating synthesized by electron-beam physical vapor deposition and a model $33\text{CaO}-9\text{MgO}-13\text{AlO}_{3/2}-45\text{SiO}_2$ (CMAS) melt with a melting point of $\sim 1240^\circ\text{C}$ was investigated. A dense, fine-grained, $\sim 6\ \mu\text{m}$ thick reaction layer formed after 4h of isothermal exposure to 1300°C . It consisted primarily of an apatite phase based on $\text{Gd}_8\text{Ca}_2(\text{SiO}_4)_6\text{O}_2$ and fluorite ZrO_2 with Gd and Ca in solid solution. Remarkably, melt infiltration into the intercolumnar gaps was largely suppressed, with penetration rarely exceeding $\sim 30\ \mu\text{m}$ below the original surface. The microstructural evidence suggests a mechanism in which CMAS infiltration is arrested by rapid filling of the gaps with crystalline reaction products, followed by slow attack of the column tips.

Submitted to Journal of the American Ceramic Society, March 21, 2007

Keywords: corrosion/corrosion resistance, infiltration, rare earths, silicates, zirconate

[†] Research sponsored by the Office of Naval Research under contracts N00014-99-1-0471 and MURI/N00014-00-1-0438, monitored by Dr. David Shifler. The project benefited from the use of the UCSB-MRL Central Facilities supported by NSF under award No. DMR00-80034.

[§] Corresponding author, skraemer@engineering.ucsb.edu

^{*} Member, American Ceramic Society

I. Introduction

Rare-earth zirconates (REZ) have generated substantial interest as novel thermal barrier coatings (TBC) based primarily on their intrinsically lower thermal conductivity and higher resistance to sintering than the state-of-the-art $\text{ZrO}_2\text{-7wt.\%Y}_2\text{O}_3$ (7YSZ) [1-4]. In addition, the pyrochlore zirconates ($\text{RE}_2\text{Zr}_2\text{O}_7$) are stable as single phases at all relevant temperatures, from $\leq 1550^\circ\text{C}$ for $\text{Gd}_2\text{Zr}_2\text{O}_7$ [5] to $\leq 2300^\circ\text{C}$ for $\text{La}_2\text{Zr}_2\text{O}_7$ [6], circumventing the phase stability problem that ultimately limits the temperature capability of 7YSZ [7]. In principle, this combination of attributes should enable higher gas path temperatures with a comparable coating thickness while maintaining the metal surface within allowable limits.

Increases in operating temperature associated with current TBC technology have clear benefits in engine efficiency [8] but also unintended consequences by introducing new modes of coating degradation that threaten further progress. Of particular interest to aircraft engines is the ingestion of siliceous particulate (dust, sand, volcanic ash, runway debris) with the intake air [9]. At lower temperatures these particles may impact the airfoil surfaces and cause erosive wear or local spallation of the TBC [10-12]. As engine temperatures rise, the finer debris tends to adhere to the coating surface [13] and form calcium magnesium alumino-silicate (CMAS) melts that penetrate the open void spaces in the coating [9]. Upon cooling at the end of an operation cycle the melt freezes and the infiltrated volume of the coating becomes rigid, losing its ability to accommodate strains arising from the thermal expansion mismatch with the underlying metal. The coating develops delamination cracks that lead to its progressive exfoliation with concomitant loss of insulation efficiency and accelerated degradation of the metallic layers underneath [14]. Concurrent with the thermomechanical damage 7YSZ coatings undergo significant chemical attack by the CMAS melt [9, 15].

The present investigation addresses the potential effect of CMAS on $\text{Gd}_2\text{Zr}_2\text{O}_7$ (GZO) as a candidate higher-temperature TBC material. The focus is on coatings produced by electron-beam physical vapor deposition (EB-PVD) but similar phenomena are expected to occur in those deposited by atmospheric plasma spray (APS). The results are discussed in the context of recent studies of a similar nature on 7YSZ [15, 16].

II. Experimental procedures

$\text{Gd}_2\text{Zr}_2\text{O}_7$ was deposited on polycrystalline alumina substrates ($25 \times 25 \times 0.6\text{mm}$, 99.5% purity, CoorsTek) using an in-house dedicated EB-PVD facility [17] fed with pre-alloyed ingots (Trans-Tech, Adamston, MD). Ceramic substrates were selected to facilitate heating the system isothermally above the melting point of the CMAS ($>1200^\circ\text{C}$), which would cause excessive degradation of superalloy substrates. One important difference with 7YSZ is that $\text{Gd}_2\text{Zr}_2\text{O}_7$ tends to react with Al_2O_3 to form a GdAlO_3 interphase, as reported elsewhere [18]. However, the times involved in the present experiments were relatively short and in practice did not to unduly compromise the coating adherence. $200\ \mu\text{m}$ thick coatings were deposited at $\sim 2\ \mu\text{m}/\text{min}$ on substrates held at 1000°C and mounted on a tubular ceramic holder rotating over the source at a rate of 8 rpm, as described elsewhere [17].

A model CMAS composition of 35CaO-10MgO-7Al₂O₃-48SiO₂ (all in mole percent) or C₃₃M₉A₁₃S₄₅ (in atomic percent cation) was selected for consistency with prior studies. It was based on the average of melts found to have penetrated TBCs on turboshaft shrouds operated in a desert environment [9], excluding the minor components believed to originate mainly from the engine (Fe and Ni). Earlier work revealed that this composition starts to melt at approximately 1235°C when made from the constituent oxides, is completely molten at 1240°C and remains amorphous upon cooling [15]. The model CMAS was prepared by mixing reagent-grade fine powders of the individual oxides and milling them in water to form a thick paste, which was subsequently applied to the surface of the TBC specimens well in excess of the amount needed to infiltrate all the porosity in the coating ($\sim 8\ \text{mg}/\text{cm}^2$). After drying, the specimens were heated to 1300°C for 4h with ramp up and down rates of $6^\circ\text{C}/\text{min}$.

Cross sections of the specimens exposed to CMAS were cut along a plane perpendicular to the rotation axis. These were embedded in epoxy and subsequently polished for examination by scanning electron microscopy (SEM) in both secondary (SE) and back-scattered electron (BSE) imaging modes. Transmission electron microscopy (TEM) specimens were cut from selected areas of the polished cross sections using a focused ion beam (FIB). This technique is particularly advantageous in the present specimens because it allows precise sampling of locations exhibiting specific microstructural features or reaction products. TEM analysis included bright

field (BF), dark field (DF), high-angle annular dark-field (HAADF) imaging, as well as selected area diffraction (SAD) and energy dispersive X-ray spectroscopy (EDS).

III. Results

The first sign that gadolinium zirconate reacts significantly differently to the CMAS exposure than 7YSZ was immediately evident on the macroscopic scale. CMAS on 7YSZ heated to 1300°C penetrated quickly and locally the TBC and spread laterally within the coating, leaving behind a shallow glassy droplet completely contained within the limits of the original deposit—Fig. 1(a). When applied to the GZO TBC under the same conditions the CMAS melt spread over the entire sample leaving a continuous layer with a flat glassy surface—Fig. 1(b). Cross sectional examination revealed the CMAS layer to be $\sim 30\ \mu\text{m}$ thick. At the boundary between CMAS and TBC the originally pointed column tips had been replaced by a $\sim 6\text{--}8\ \mu\text{m}$ thick layer of reaction products with seemingly crystalline protrusions extending into the CMAS (Fig. 2). The intermediate contrast of the reaction product in BSEI is consistent with the incorporation of lighter elements from the CMAS (darker) and heavier elements from the GZO (brighter).

The most striking observation was that the CMAS melt infiltrated the inter-columnar porosity in GZO only to a depth of $\leq 30\ \mu\text{m}$ below the original TBC surface after a 4h exposure (Fig. 2), whereas full penetration occurs within minutes in 7YSZ under the same conditions [15]. In some locations CMAS penetrated no further than the lower boundary of the reaction layer in the neighboring columns. The distinction between open and infiltrated porosity is clearly made by combining SE and BSE imaging of the same area (Fig. 3). The inset in Fig. 3(a) also reveals traces of CMAS within the fine feathery porosity surrounding an otherwise empty intercolumnar pore beneath the main infiltration front, suggesting preferential spreading along the column walls. However, this effect is limited to a few micrometers with no evidence of CMAS found in the lower three quarters of the TBC thickness.

The thermochemical interaction between GZO and CMAS is arguably linked to the arrest of the CMAS infiltration and thus deserves further analysis. Closer examination of the reaction layer in Fig. 2 reveals a modulated structure with periodicity dictated by the intercolumnar spacing (Fig. 4). The microstructure can be conveniently divided into three types of regions. The first one is associated with the former intercolumnar gaps, which are now filled with reaction products and

extend into the bulk reaction layer leaving an intriguing “ghost” trace as denoted by the arrow in Fig. 4. These regions appear to show little or no residual CMAS relative to the rest of the reaction layer, and retain features reminiscent of the feathery pattern within the partially penetrated gaps. The second type of microstructure within the reaction layer corresponds to the locations formerly occupied by column tips, which show a graded structure consisting of crystalline reaction products within an interpenetrating CMAS network. Both the relative amount of CMAS and the scale of the crystalline products decrease toward the interface between the reaction layer and the residual GZO, becoming irresolvable at the scale of the image in Fig. 5. The third and uppermost part of the reaction layer consists primarily of large acicular faceted crystals protruding into the residual CMAS on top of the coating, interspersed with non-faceted globular particles.

Microstructural and microchemical characterization of the reaction layer was undertaken by TEM analysis of FIB samples extracted from the locations schematically illustrated in Fig. 4. The issues of interest were (i) the identification of the reaction products, (ii) the structure of the infiltrated column gaps, both between remaining columns as well as within the reaction zone, (iii) the constitution and morphology of the reaction zone above a column core, and (iv) the interface between the latter and the residual GZO.

The nature of the larger needles was investigated on a FIB lamella from location A in Fig. 4, whose bright field image is shown in Fig. 5. Electron diffraction revealed a structure with hexagonal symmetry and lattice constants $a=9.5\text{\AA}$ and $c=6.9\text{\AA}$, while TEM/EDS analysis suggested a silicate containing Gd, Ca and a smaller amount of Zr (Table I). The evidence is consistent with an apatite-type phase similar to $\text{La}_8\text{Sr}_2\text{Si}_6\text{O}_{26}$ [19], which has been studied extensively owing to its potential as a solid oxide ion conductor [20]. The long axes of the needles are parallel to the [0001] direction of the apatite unit cell, while the facets bounding the transverse sections are of the $\{10\bar{1}0\}$ type. The amorphous matrix in Fig. 5(a) is CMAS modified with small amounts of Gd and Zr in solid solution (Table I).

The structures along sections C and B in Fig. 4, corresponding to an infiltrated gap and its “ghost” extension into the bulk reaction zone, are depicted together with their surroundings in Fig. 6. The denser region in the middle of Fig. 6(a) is the former intercolumnar gap filled with reaction products, while the neighboring regions correspond to the microstructure within a former column tip. Both areas contain a mixture of apatite crystals of composition similar to the

larger needles in the upper reaction zone and a fluorite phase containing Zr, Gd and some Ca in solid solution (Table I). However, while the region above the column core contains significant amounts of a residual glassy phase (darker pockets), much less is present in the former intercolumnar gap. Where surrounded by CMAS the apatite and fluorite crystals can be readily distinguished by the faceted boundaries of the former and more globular appearance of the latter. That difference is less evident within the intercolumnar gap “ghost”, where apatite crystals appear to be more abundant.

TEM analysis of section C in Fig. 4, taken 2 μm below the lower boundary of the reaction zone at the same column gap as in section B, revealed a continuous chain of apatite grains between the two columns—Fig. 6(b). The specimen in this figure was tilted so that both columns were close to the $\langle 100 \rangle$ zone axis, corresponding to the texture induced by the deposition conditions [21]. The strong diffraction condition darkened the columns and enhanced the visibility of the apatite phase (a) in the channel. Protrusions (z') extending from the column cores into the apatite phase were identified as fluorite ZrO_2 with a higher $\text{GdO}_{1.5}$ content (20-30%) than in the upper reaction layer (~13%) but a similar amount of CaO (~3%). The diffraction contrast in Fig. 6(b) indicates that the fluorite protrusions grew epitaxially onto the parent column. Small pockets of other phases noted in Fig. 6(b) were identified as spinel and residual crystallized CMAS.

The variation in microstructure above the column core with distance from the GZO interface is shown in Fig. 7. The micrographs correspond to in-plane sections taken at distances of 5 μm , 2 μm and 800 nm from the interface with the remaining GZO column. The relative amount of CMAS clearly decreases toward the interface, forming a thin grain boundary phase with small pockets at grain corners in the lower parts of the reaction layer, Fig. 7(b), which appears rather indistinct in Fig. 4. The scale of the reaction products also decreases with distance from the interface, from ~400 nm at 5 μm , Fig. 7(a), to ~100 nm at 800 nm, Fig. 7(c). The faceted nature of the apatite grains becomes less distinct closer to the interface, and the fluorite particles become less globular and meander around the apatite crystals, as illustrated in Fig. 7(c), similar to the protrusions in the intercolumnar gaps—Fig. 6(b). The Gd content in the fluorite was found to increase from ~13% at the 5 μm level to ~24% 800 nm above the interface whereas the Ca:Gd ratio in the apatite decreases concomitantly from 0.4 to 0.25 (Table I). Area analysis suggested approximately equal amounts of fluorite and apatite near the interface.

A FIB TEM lamella cut along location D in Fig. 4 revealed a structure of elongated grains within the reaction zone closest to the interface (Fig. 8). The grains, ~50 nm wide, comprise alternating apatite and fluorite phases, the latter with up to ~30%GdO_{1.5} and ~2%CaO. The composition of GZO directly underneath the interface shows no deviation from bulk values. Thin dark lines in the Z-contrast image of Fig. 8 denote amorphous grain boundary films, which are distinguishable down to ~200 nm above the interface. No amorphous phase was detected at the interface, possibly because of the associated roughness. However, dark field analysis showed no evidence of epitaxial relationships between the parent GZO and the product fluorite (Fig. 9) such as those observed in the column gaps, allowing the possibility of a thin amorphous film at the interface. Figure 9 also shows that the growth of the apatite and fluorite phases near the interface is columnar, suggesting a cooperative mechanism. Diffraction analysis reveals that the apatite grains are textured with a preferred [0001] orientation that is tilted relative to the primary $\langle 100 \rangle$ axis of the GZO column but aligned approximately with the interface normal.

IV. Discussion

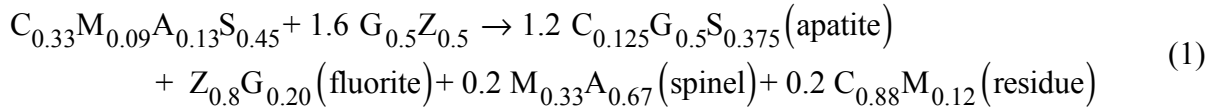
The crucial finding of this work is that CMAS infiltration into a columnar GZO TBC (and arguably any APS analog) can be largely suppressed *even in the absence of a thermal gradient* across the coating. To the limited extent that the intercolumnar channels were penetrated, typically $\leq 30\mu\text{m}$ from the original coating surface, they were filled with a mixture of predominantly crystalline phases. This is in striking contrast with the results of identical experiments on 7YSZ coatings, where the channels were completely filled by amorphous CMAS with only minor amounts of Zr and Y in solid solution [15].

The observations are consistent with a scenario wherein CMAS infiltration into GZO is suppressed by crystallization occurring concurrently with the inward flow of the silicate melt and *at temperatures above the melting point of the original CMAS deposit* (~1240°C). This is obviously possible only if (i) the CMAS composition is dynamically modified by dissolution of the base GZO material as it penetrates into the coating, (ii) the characteristic time scales of the penetration, dissolution and crystallization kinetics are all comparable, and (iii) the process consumes a large fraction of the melt and yields sufficient volume of crystalline product to fill the gap close to the surface and preclude further percolation downward. (Possible effects of the modified

composition on the viscosity and wetting ability of the melt are discussed later). It is therefore important to understand first the chemical interaction between CMAS and GZO and the nature of the reaction products.

(1) Reaction Products and Mass Balance

As a first approximation the chemical reaction between the model CMAS and stoichiometric GZO may be written as:



where the oxides are identified by the cation first letter and all formulae are given on the basis of one gr-atom of cations. There are three distinct crystalline products (apatite, fluorite and spinel) written here in their simplest form, and some residue to be discussed later.

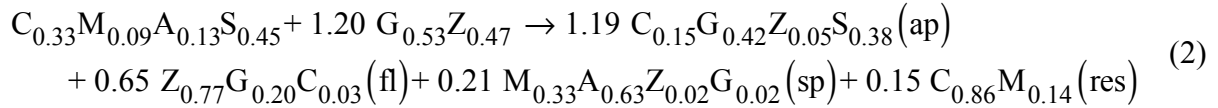
The key product is the apatite phase (*hexagonal*, $P\bar{3}$ [19, 20]), nominally based on $Gd_8Ca_2(SiO_4)_6O_2$ which melts congruently at 1930°C [22]. The structure consists of isolated (SiO_4) tetrahedra arranged around two types of channels running parallel to the *c*-axis [20]. The larger of these channels, passing through the origin, contains a row of ionic O along its axis surrounded by cations that are coordinated by 7 anions (heretofore 7C sites). Analyses of related structures suggest these sites to be predominantly occupied by Gd^{3+} [20, 23]. The smaller channels contain rows of alternating Ca^{2+} and Gd^{3+} at their center, each coordinated by 9 anions from the covalently bonded SiO_4 tetrahedra (9C sites). The apatite formula may thus be re-written as $Gd_6[Gd_2Ca_2](SiO_4)_6O_2$, where cations in square brackets are 9C, those outside are 7C, and the ionic O is explicitly distinguished from that tied to Si tetrahedral units. The distinction between the sites is relevant to understanding the observed deviations from the apatite stoichiometry (Table I).

Apatite is the only intermediate compound in the quasibinary $CaSiO_3$ - Gd_2SiO_5 [22], where it exhibits a finite homogeneity range $Gd_{2x}Ca_{(1-x)}(SiO_4)O_{2x-1}$, with $0.6 \leq x \leq 0.75$ at 1300°C. Studies in related structures suggest that excess Ca ($0.6 \leq x \leq 2/3$) is accommodated by substitution for Gd in the 9C sites, with concurrent creation of vacancies in the ionic O lattice. Conversely, excess Gd is likely to substitute for Ca on 9C sites with concomitant creation of vacancies in that same lattice. This view is supported by the site occupancies in the defect apatite $La_{9.33}(SiO_4)_6O_2$

[19] also formed by Nd [24], Gd [25] and Dy [23]. Interestingly, those silicates show substantial solubility of Al [24]; but no significant Al was detected in the present crystals even though they grow from an Al-bearing melt. Instead, they incorporate Zr^{4+} (Table I), presumably in the 7C sites given the smaller size of this ion relative to Gd^{3+} and Ca^{2+} and its preferred coordination in ZrO_2 [26]. Measured Ca:Gd ratios vary from 0.45 to 0.25, the latter corresponding to the stoichiometric apatite. The excess Ca^{2+} helps compensate for the higher Zr^{4+} charge so that fewer anion or cation vacancies need to be created, with attendant benefits to the stability of the structure. Because the measured Zr^{4+} is generally in excess of the amount that can be compensated by the Ca^{2+} , the apatite of interest is likely to contain vacant 9C sites, whereupon its formulation becomes $Gd_{6-y}Zr_y[Gd_{2-(2z+y)/3}Ca_{2+z}](SiO_4)_6O_2$ ($y \geq z$). Taking average concentrations of 15%CaO and 5% ZrO_2 the corresponding Si and Gd contents are ~38% and ~42%, respectively, reasonably close to the measured compositions (Table I). The corresponding site occupancy would imply that ~3% of the 9C sites are vacant.

Because the apatite has a much higher Gd:Zr ratio than GZO, the observed ZrO_2 -rich fluorite is expected from mass balance considerations. This phase is found to incorporate Gd over a wide composition range (0.12-0.3 $GdO_{1.5}$), but always as a minor component, as well as a small amount of Ca (0.03-0.04CaO). In that respect the reaction is similar to that with 7YSZ in which the TBC dissolves to precipitate a tetragonal phase with lower Y and some Ca incorporated from the CMAS melt [15]. That process, however, does not yield other crystalline products and the excess Y simply remains in solid solution in the residual amorphous CMAS, whose composition does not change significantly. In contrast, the substantial depletion of Ca and Si from the melt when reacting with GZO to form apatite and the apparent inability of apatite and fluorite to incorporate significant amounts of Mg or Al lead to the supersaturation of these oxides in the melt and their precipitation as spinel, the third crystalline product of the reaction. This is fully consistent with the expected melt evolution path in the quaternary liquidus projection of the CaO-MgO- Al_2O_3 - SiO_2 system (Fig. 2647 in [27]). The small amounts of Zr and Gd detected in the spinel presumably substitute for Al on octahedral sites.

Considering now the actual compositions of the different phases, on average, the balanced reaction may be rewritten as:



Note that the yield of crystalline products is 93% of the reactants on a molar basis. Given molar volumes (in cm³ per gr-atom of cations) of 20.7 (CMAS), 20.3 (apatite), 22.1 (GZO), 20.8 (fluorite), and 13.3 (spinel),¹ the volumetric yield of the reaction excluding the residue is ~86%, just below the typical threshold for percolation. This is evidently an underestimate since the residue is diluted by additional reactants as indicated by the measured compositions of fourth phase pockets in the reaction zone. Nevertheless, the reaction does lead in practice to the sealing of the intercolumnar gaps probably because the “residual” CMAS observed in them is also crystalline. A comparison of reactions (1) and (2) indicates that the incorporation of Zr⁴⁺ into the apatite significantly reduces the amount of GZO that needs to be dissolved to produce the same volume of this crucial phase and, in principle, to seal the gaps. The broader aspects of the sealing mechanism and its interplay with the above reaction are now examined.

(2) The Infiltration-Inhibiting Mechanism

The microstructure of the reaction zone appears to have evolved in two major stages, as schematically illustrated in Fig. 10. The first one involves the sealing of the intercolumnar gaps soon after the deposit starts melting and the first liquid begins to flow into the coating. The mechanism is one of rapid dissolution of the GZO upon contact with the melt and nearly concurrent precipitation of multiple crystalline phases following approximately reaction (2). The very limited penetration suggests that the infiltration rate may be initially controlled by the availability of melt, and hence by the melting kinetics, rather than by the resistance to capillary-driven flow into a porous bed from a liquid reservoir at the surface, as assumed in the 7YSZ study [15]. (The details are not as critical in 7YSZ because the dissolution/re-precipitation process does not change significantly the volume of the melt or its flow/crystallization behaviors.) The envisaged process starts with the incipient melt trickling down the sides of the column gap, infiltrating the feathery porosity and thus the surface exposed to dissolution, and at some point downstream nucleating the apatite phase—Fig. 10(a). Whether the fluorite phase might nucleate upstream at an earlier

¹ Molar volumes were calculated from the CMAS density measured in [15], and for the crystalline materials from the compositions in reaction (2) and lattice parameters for apatite from this work, and for the zirconate, fluorite and spinel phases from the literature [28, 29].

time is not critical to the apatite formation since its volume would be smaller than that of the dissolved GZO and would still lead to a net increase in the Gd content of the melt. The apatite crystals could nucleate within the melt and travel downstream until they get trapped at a narrow point in the channel, or heterogeneously on the column surfaces. The same process arguably occurs within the feathery pores, limiting the penetration of the melt into the column core although factors such as pore breakdown upon thermal exposure could play an equally important role. As more melt trickles into the channel and additional apatite and fluorite form, both the area available for flow and volume of melt decrease until the latter freezes into a mixture of spinel and residual aluminosilicate hindering further penetration—Fig. 10(b).

The melt-starved infiltration scenario has two important implications: (i) it makes the dissolution and crystallization processes more competitive with the infiltration kinetics, and (ii) because the incipient melt is unlikely to have the composition of the bulk CMAS the relative proportions of crystalline products in reaction (2) could be different, presumably accounting for the smaller amounts of the spinel and residual CMAS observed in practice. (Sampling statistics, always an issue in TEM, could obviously play a role too.) Elucidation of these early infiltration stages is the subject of ongoing research and will be reported in a subsequent paper.

(3) Reaction with the Column Tips

The “ghost” traces of the intercolumnar gaps within the main reaction layer suggest that their filling with crystalline products occurred very early in the process, while the column tips had experienced only minimal attack. Once the channels are blocked the increasing volume of melt spreads laterally covering the entire surface as noted in Fig. 1(a). The second major stage in the reaction mechanism thus involves the recession of the column tips as a result of further reaction with the melt—Fig. 10(c). The larger volume of melt above the TBC, relative to that within the channels, is believed to hinder the formation of a dense “barrier” layer equivalent to the structure formed between columns, since it never becomes sufficiently saturated to crystallize completely. Indeed, no spinel or crystalline residual CMAS were found in the microstructure above the column cores, leaving a volume of melt through which the transport necessary for additional dissolution could take place.

The above scenario is broadly similar to the attack of the column tips on 7YSZ under similar conditions [15], with some important differences. The upper reaction zone in 7YSZ comprises loose agglomerates of t-ZrO₂ globules embedded in a CMAS matrix sufficiently abundant to allow substantial contact with the underlying columns and the persistence of the dissolution-reprecipitation process. In contrast, the reaction with the GZO tips generates a layer of alternating apatite and fluorite elongated grains with an intergranular amorphous phase that becomes progressively thinner near the interface with the remaining GZO column core (Figs. 7-9). The transport of species needed to sustain the reaction, i.e. Ca and Si toward the interface, and excess Zr and Gd away from it, presumably takes place through this amorphous phase. Whether the latter extends to the interface, as suggested by the absence of a crystallographic relationship between GZO and the fluorite growing from it, and mediates the reaction is yet to be ascertained.

The details of the *column core attack* are still under investigation and are not essential to the main subject of this paper, i.e. the mechanism by which access of the CMAS melt to the majority of the pore space in the coating is impeded. The recession of the column cores arguably takes place over a much longer time scale than the sealing of the gaps. The structure of the near interface layer suggests that the rate decreases over time and becomes controlled by diffusion through the network of amorphous boundary films. The interfacial reaction apparently yields phases with compositions that are not fully compatible with the melt above, notably a higher Gd content in the fluorite phase. Away from the interface the phases experience melt mediated coarsening, adjusting their composition in the process. The larger acicular crystals at the top could evolve partially under these conditions but probably develop their elongated shape as a result of additional growth upon cooling—Fig. 10(d). Remarkably, the “ghost” microstructure produced by the earlier reaction within the intercolumnar gaps remains substantially unaltered, as seen in Fig. 4. This resilience is probably the result of phase compositions that are closer to equilibrium with the melt, and the absence of significant amounts of percolating amorphous phase as shown, for example, in Fig. 6(a). Whether some melt penetration and coarsening may occur near the surface, as suggested by Fig. 4, is not particularly critical as long as the gaps remain sealed further down. It is of some concern that the recession front might reach the bottom of the filled length within a gap and melt could leak down the coating, but this appears unlikely once the dense in-

terfacial layer develops, as indicated by the open gaps right next to the bottom of the reaction layer in Figs. 2 and 3.

(4) Additional considerations

Various other aspects of the CMAS-GZO interaction and its potential effect on the infiltration-governing parameters merit discussion. Modifications to the wetting characteristics of the CMAS melt by the dissolved Gd and Zr are undoubtedly possible, but experimental evidence suggests that the observed behavior is not due to diminished wetting ability. Indeed, the melt spreads over nearly the entire coating, Fig. 1(a), and it readily penetrates the fine feathery pores on the column sides. Fig. 3(a). It also wets the reaction products, as evident in Figs. 7 and 8. A more likely effect of the dissolved species could be on the viscosity of the melt and the ensuing inward flow. There are documented effects of rare earth additions increasing the viscosity of aluminosilicate glasses [30] but the latter contained no other modifiers like Ca or Mg and much higher concentrations of RE in the melt. Conversely, the crystallization of apatite would increase the Ca:Si ratio in the melt, decreasing the connectivity of the network and, in principle, its viscosity. Arguably, the effects of the dissolution of GZO into the CMAS in promoting crystallization of the melt are more important than those on the melt viscosity.

Finally, the potential of the infiltration-inhibiting reaction needs to be assessed in the context of more realistic conditions. The thermal gradient across the coating in actual engine operation should further limit the penetration, as it does in 7YSZ [15], subject to the constraint that sufficient dissolution must take place for the melt to crystallize and fill the gaps. Conversely, engine operation involves thermal cycling, and hence the resistance of the reacted/infiltrated layer to delamination is a critical issue requiring evaluation. While the modified layer is substantially thinner than those observed in actual 7YSZ TBCs, the toughness of GZO is significantly lower [21] and the thermal expansion properties of the reaction products are not known. The CTE for the fluorite phase is probably similar to that of GZO ($11.6 \text{ ppm}\cdot\text{K}^{-1}$ [28]) but literature for other silicate oxyapatites suggests that their CTE's tend to be significantly lower and anisotropic, e.g. $8.9 \text{ ppm}\cdot\text{K}^{-1}$ and $6.6 \text{ ppm}\cdot\text{K}^{-1}$ along the a and c axes, respectively, for the closely related $\text{La}_8\text{Ca}_2(\text{SiO}_4)_6\text{O}_2$ [31]. It is then possible that the thermal characteristics of the reaction products may partly counteract the benefits of the reduced penetration. These issues are under current investigation.

V. Conclusions

The current investigation has shown that the propensity of CMAS to react with most thermal barrier oxides of interest can be manipulated by careful selection of the coating material to mitigate the penetration of the compliance-inducing features of the microstructure and the detrimental effects on the strain tolerance of the coatings. Gd zirconate has proven to be effective in this manner, and the details of the reaction suggest that other rare earth zirconates may behave similarly. In essence, the mitigation mechanism relies on the dissolution of the zirconate into the melt and the ensuing conversion of the latter into a mixture of crystalline phases that fill the flow channels and prevent further penetration. The extent of penetration depends on the relative competitiveness of the infiltration, dissolution and crystallization kinetics, all of which should be dependent on temperature and the compositions of the melt and oxide material. Key to the effectiveness of the mechanism is the formation of a highly stable apatite phase incorporating Ca, Gd, Si and some Zr. After the early sealing of the flow channels the reaction continues slowly by interaction of the bulk CMAS with the column tips. The mechanism and product morphology are conducive to a progressive slowing of this attack, which is beneficial to the survivability of the reaction layer under thermal cycling. Further research on the mechanisms and assessment of the effectiveness of this mitigation approach is in progress.

Acknowledgments

The authors would like to thank Dr. D. Klenov (UCSB) for his guidance in Z-contrast imaging. Helpful discussions with Dr. M. Maloney (Pratt & Whitney) and Prof. A.G. Evans (UCSB) are gratefully acknowledged.

References

1. M.J. Maloney, "Thermal barrier coating systems and materials," U.S. Patent 6,117,560, 2000.
2. R. Vassen, X. Cao, F. Tietz, D. Basu, and D. Stöver, "Zirconates as new materials for thermal barrier coatings," *Journal of the American Ceramic Society*, 83 [8] 2023-2028 (2000).
3. M.J. Maloney, "Thermal barrier coating systems and materials," U.S. Patent 6,177,200, 2001.
4. R. Subramanian, "Thermal barrier coating having high phase stability," U.S. Patent 6,258,467, 2001.
5. S.M. Lakiza, O. Fabrichnaya, C. Wang, M. Zinkevich, and F. Aldinger, "Phase diagram of the ZrO_2 - Gd_2O_3 - Al_2O_3 system," *Journal of the European Ceramic Society*, 26 233-246 (2006).
6. A. Rouanet, "Contribution a l'etude des systèmes zircone-oxydes des lanthanides au voisinage de la fusion," *Rev. Int. Hautes Tempér. et Réfract.*, 8 [2] 161-180 (1971).
7. C.G. Levi, "Emerging Materials and Processes for Thermal Barrier Systems," *Current Opinion in Solid State and Materials Science*, 8 [1] 77-91 (2004).
8. R.L. Jones, "Thermal barrier coatings", p. 194-235 in *Metallurgical and Ceramic Protective Coatings*. Edited by K.H. Stern. Chapman & Hall: London, 1996.
9. M.P. Borom, C.A. Johnson, and L.A. Peluso, "Role of environmental deposits and operating surface temperature in spallation of air plasma sprayed thermal barrier coatings," *Surface and Coatings Technology*, 86-87 116-126 (1996).
10. J.R. Nicholls, R.G. Wellman, and M.J. Deakin, "Erosion of Thermal Barrier Coatings," *Materials at High Temperatures*, 20 [2] 207-218 (2003).
11. X. Chen, M.Y. He, I.T. Spitsberg, N.A. Fleck, J.W. Hutchinson, and A.G. Evans, "Mechanisms governing the high temperature erosion of thermal barrier coatings," *Wear*, 256 [7-8] 735-746 (2004).
12. A.G. Evans, N.A. Fleck, S. Faulhaber, N. Vermaak, M. Maloney, and R. Darolia, "Scaling laws governing the erosion and impact resistance of thermal barrier coatings," *Wear*, 260 886-894 (2006).
13. J.L. Smialek, F.A. Archer, and R.G. Garlick, "Turbine airfoil degradation in the Persian Gulf war," *JOM*, 46 [12] 39-41 (1994).
14. C. Mercer, S. Faulhaber, A.G. Evans, and R. Darolia, "A delamination mechanism for thermal barrier coatings subject to calcium-magnesium-alumino-silicate (CMAS) infiltration," *Acta Materialia*, 53 [4] 1029-1039 (2005).
15. S. Krämer, J.Y. Yang, C.A. Johnson, and C.G. Levi, "Thermochemical interactions of thermal barrier coatings with molten CaO - MgO - Al_2O_3 - SiO_2 (CMAS) deposits," *Journal of the American Ceramic Society*, 89 [10] 3167-3175 (2006).
16. S. Faulhaber, S. Krämer, M. Chambers, D.R. Clarke, C.G. Levi, J.W. Hutchinson, and A.G. Evans, "Mechanism of delamination in a thick thermal barrier system subject to Calcium-Magnesium-Alumino-Silicate penetration," (in preparation).
17. S.G. Terry, "Evolution of microstructure during the growth of thermal barrier coatings by electron-beam physical vapor deposition," *Doctoral Dissertation in Materials*, University of California, Santa Barbara, CA, 2001.
18. R.M. Leckie, S. Krämer, M. Rühle, and C.G. Levi, "Thermochemical compatibility between Alumina and ZrO_2 - $GdO_{3/2}$ thermal barrier coatings," *Acta Materialia*, 53 [11] 3281-3292 (2005).

19. J.E.H. Sansom, D. Richings, and P.R. Slater, "A powder neutron diffraction study of the oxide-ion-conducting apatite-type phases $\text{La}_{9.33}\text{Si}_6\text{O}_{26}$ and $\text{La}_8\text{Sr}_2\text{Si}_6\text{O}_{26}$," *Solid State Ionics*, 139 205-210 (2001).
20. J.R. Tolchard, M.S. Islam, and P.R. Slater, "Defect chemistry and oxygen ion migration in the apatite-type materials $\text{La}_{9.33}\text{Si}_6\text{O}_{26}$ and $\text{La}_8\text{Sr}_2\text{Si}_6\text{O}_{26}$," *Journal of Materials Chemistry*, 13 1956-1961 (2003).
21. R.M. Leckie, "Fundamental issues regarding the implementation of Gd zirconate in thermal barrier systems," Doctoral Dissertation in Materials, University of California, Santa Barbara, Santa Barbara, CA, 2006.
22. N.F. Fedorov, A. I.F., and T.F. Korneeva, "System $\text{CaSiO}_3\text{-Gd}_2\text{SiO}_5$," *Inorganic Materials*, 8 [12] 1919-1921 (1972).
23. S.T. Misture, S.P. Harvey, R.T. Francy, Y. Gao, S. DeCarr, and S.C. Bancheri, "Synthesis, crystal structure, and anisotropic thermal expansion of $\text{Dy}_{4.67}(\text{SiO}_4)_3\text{O}$," *Journal of Materials Research*, 19 [8] 2330-2335 (2004).
24. U. Kolitsch, H.J. Seifert, and F. Aldinger, "Phase relationships in the systems $\text{RE}_2\text{O}_3\text{-Al}_2\text{O}_3\text{-SiO}_2$ (RE = Rare Earth Element, Y and Sc)," *Journal of Phase Equilibria*, 19 [5] 426-433 (1998).
25. U. Kolitsch, H.J. Seifert, and F. Aldinger, "Phase relationships in the system $\text{Gd}_2\text{O}_3\text{-Al}_2\text{O}_3\text{-SiO}_2$," *Journal of Alloys and Compounds*, 257 [1-2] 104-114 (1997).
26. S.-M. Ho, "On the structural chemistry of zirconium oxide," *Materials Science and Engineering*, 54 23-29 (1982).
27. E.M. Levin, C.R. Robbins, and H.F. McMurdie, eds. *Phase Diagrams for Ceramists, Volume II* The American Ceramic Society: Columbus, OH, 1969.
28. M. Zinkevich, C. Wang, F.M. Morales, M. Ruhle, and F. Aldinger, "Phase Equilibria in the $\text{ZrO}_2\text{-GdO}_{1.5}$ system at 1400-1700°C," *Journal of Alloys and Compounds*, 398 261-268 (2005).
29. N.W. Grimes and E.A. Al-Ajjaj, "Low-temperature thermal expansion of spinel," *Journal of Physics: Condensed Matter*, 4 [30] 6375-6380 (1992).
30. P.F. Becher and M.K. Ferber, "Temperature-dependent viscosity of SiReAl-based glasses as a function of N:O and Re:Al ratios (RE = La, Gd, Y and Lu)," *Journal of the American Ceramic Society*, 87 [7] 1274-1279 (2004).
31. R.H. Hopkins, J. de Klerk, P. Piotrowski, M.S. Walker, and M.P. Mathur, "Thermal and elastic properties of silicate oxyapatite crystals," *Journal of Applied Physics*, 44 [6] 2456-2458 (1973).

Tables

Table I. Chemical compositions of the various constituents in the reaction zone.

Region (figure)	Constituent	CaO	MgO	AlO _{1.5}	SiO ₂	ZrO ₂	GdO _{1.5}
Upper RZ (5a, 6a)	CMAS	27 ± 2	10 ± 1	14 ± 1	43 ± 3	3	3
	Apatite	16 ± 1	-	-	37 ± 1	6 ± 1	41 ± 2
	Fluorite	4 ± 1		-	-	83 ± 1	13 ± 1
Lower RZ (7c)	Apatite	12 ± 1	-	-	37 ± 1	4 ± 1	48 ± 2
	Fluorite	3 ± 1	-	-	-	73 ± 4	24 ± 5
Infiltrated gap (6b)	Apatite	18 ± 2	-	-	38 ± 1	4 ± 1	40 ± 2
	Fluorite	3 ± 1	-	-	-	76-66	20-30
	Spinel	-	32	63	1	2	2
	CMAS	30	9	26	26	5	4
TBC (9)	GZO	-	-	-	-	47	53

All compositions are given in mol% of cations. Standard deviations of average values are given.

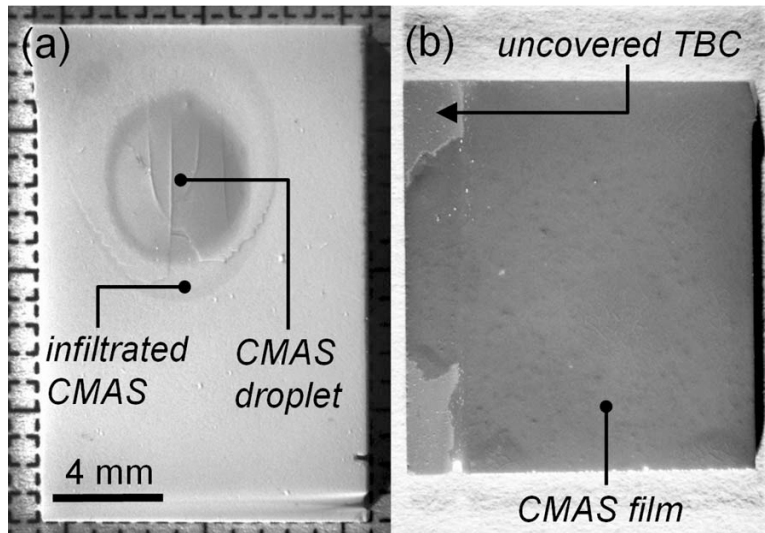


Figure 1: Optical view of TBC surfaces after CMAS attack at 1300C for 4h: (a) 7YSZ and (b) Gd zirconate. Note the distinctly different spreading behavior.

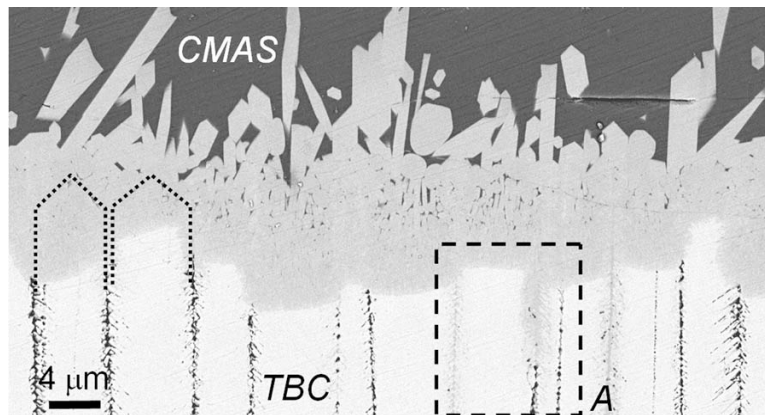


Figure 2: BSE image of the reaction zone between CMAS and a columnar GZO TBC. Dotted lines on the left illustrate the approximate shape and height of the original column structure. The area marked *A* is shown in greater detail in Fig. 3.

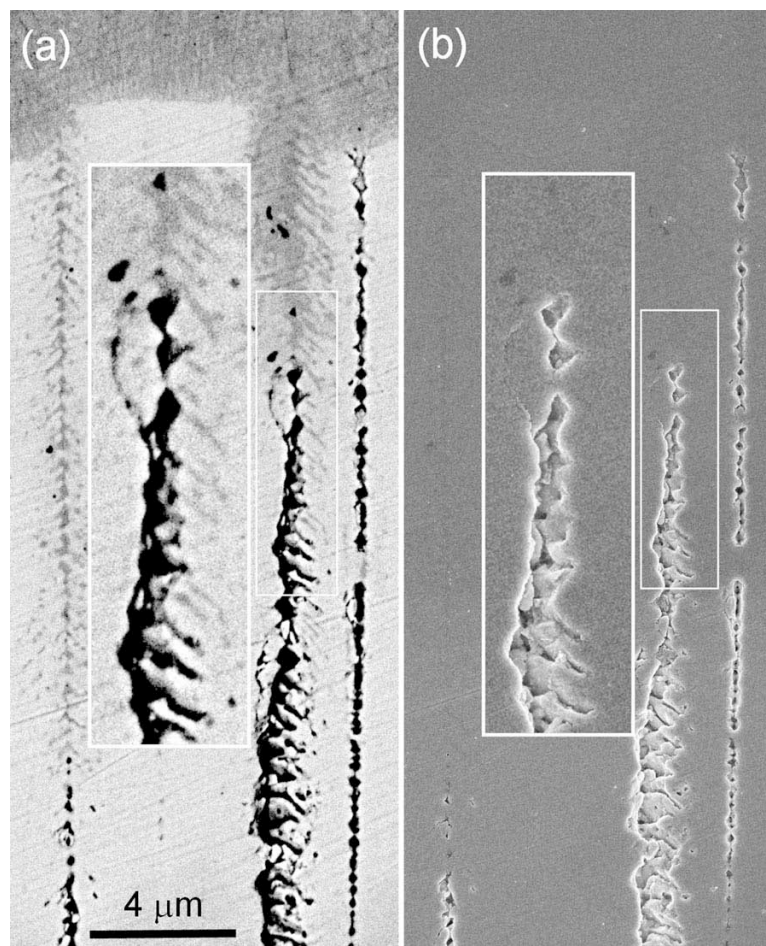


Figure 3: Identification of open v. infiltrated porosity by combining SE and BSE imaging of the same area. (a) BSE contrast reveals the infiltrated spaces when filled by the reaction product whose Z contrast is intermediate between CMAS and GZO whereas (b) SE highlights empty holes due to charging at their edges that would not be evident if the pore were filled with un-reacted CMAS. The insets are magnified (2X) views of the transition zone between filled and open porosity.

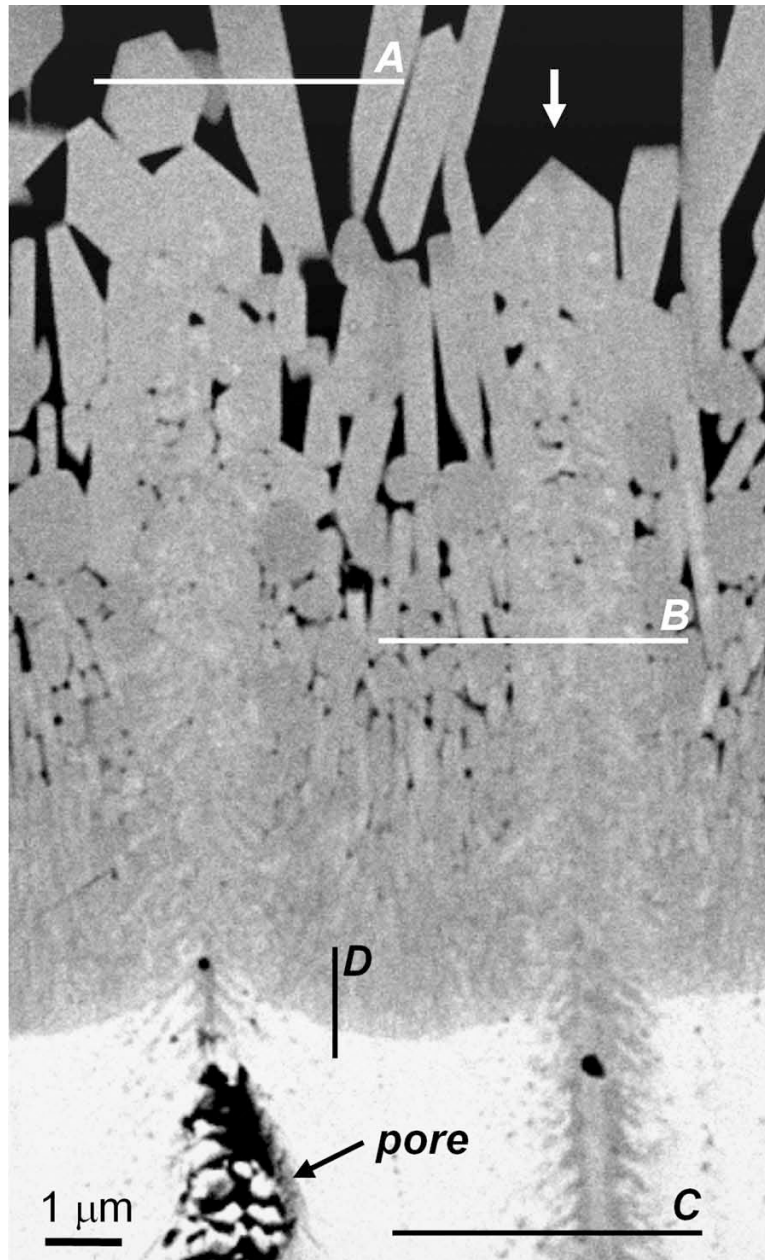


Figure 4: BSE image of the reaction zone. The imaging conditions were adjusted to maximize the contrast within the zone, which rendered the CMAS (above) indistinguishable from residual porosity (below). The lines mark positions where FIB lamellae were extracted for TEM. “B” and “C” are exact locations for the specimens shown in Fig. 6. “A” and “D” are representative positions for the microstructures shown in Fig. 5 and 7.

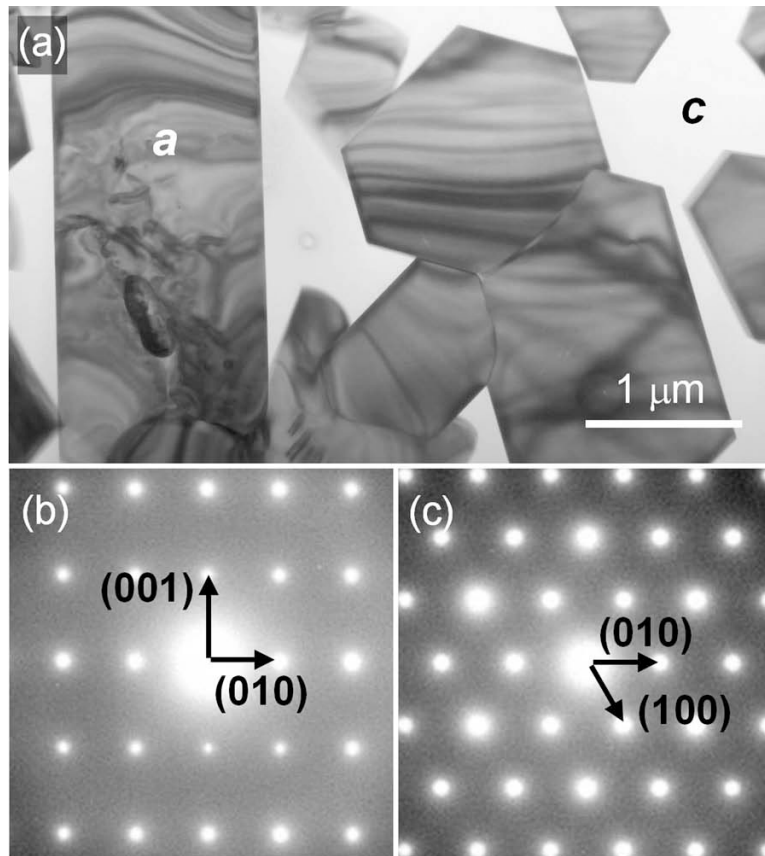


Figure 5: Bright field TEM micrograph of an area similar to A in Fig. 4, containing crystalline needles extending in various directions into an amorphous CMAS matrix. The SAD patterns correspond to the $\langle 10\bar{1}0 \rangle$ and $[0001]$ zone axes of the apatite grain marked with 'a' in (a).

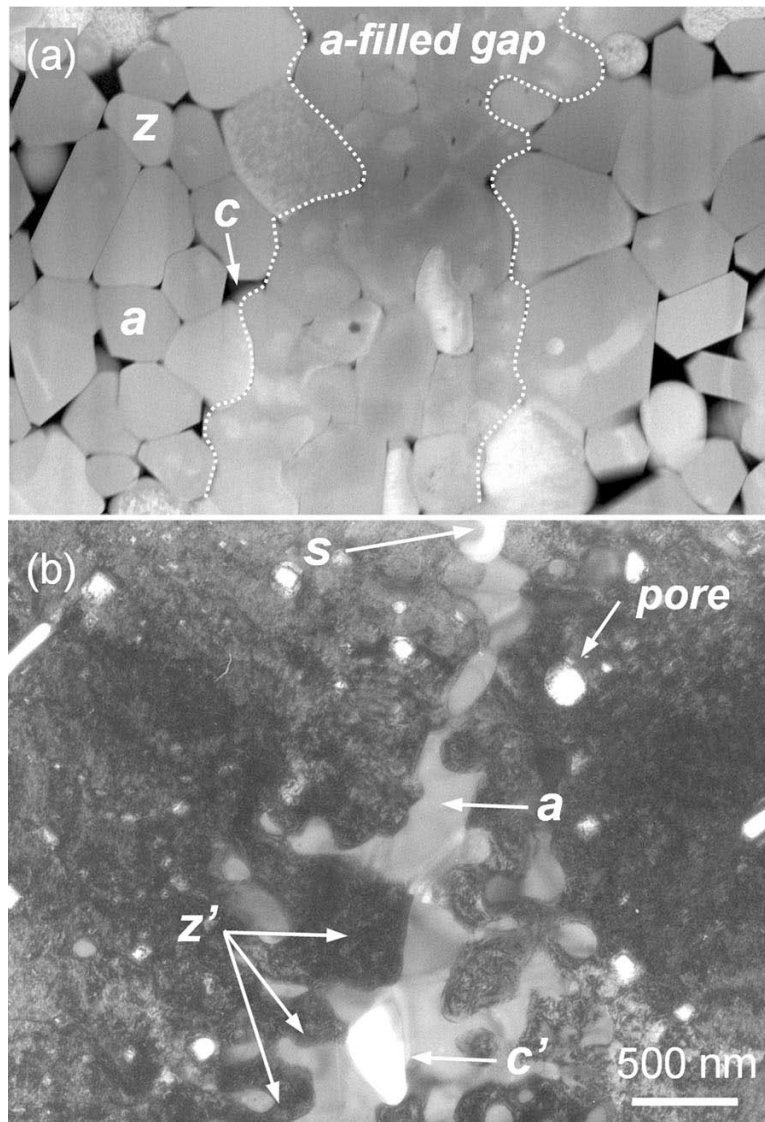


Figure 6: (a) HAADF TEM micrograph of the section marked “B” in Fig. 4. Z-contrast enables a reduction in diffraction contrast within the different grains and highlights the grain contours as well as the contrast between crystals and surrounding CMAS. (b) Bright field TEM micrograph of section marked “C” in Fig. 4. Phases: z, z' : fluorite, a : apatite, s : spinel, p : pore, c, c' : CMAS). See Table I for chemical compositions.

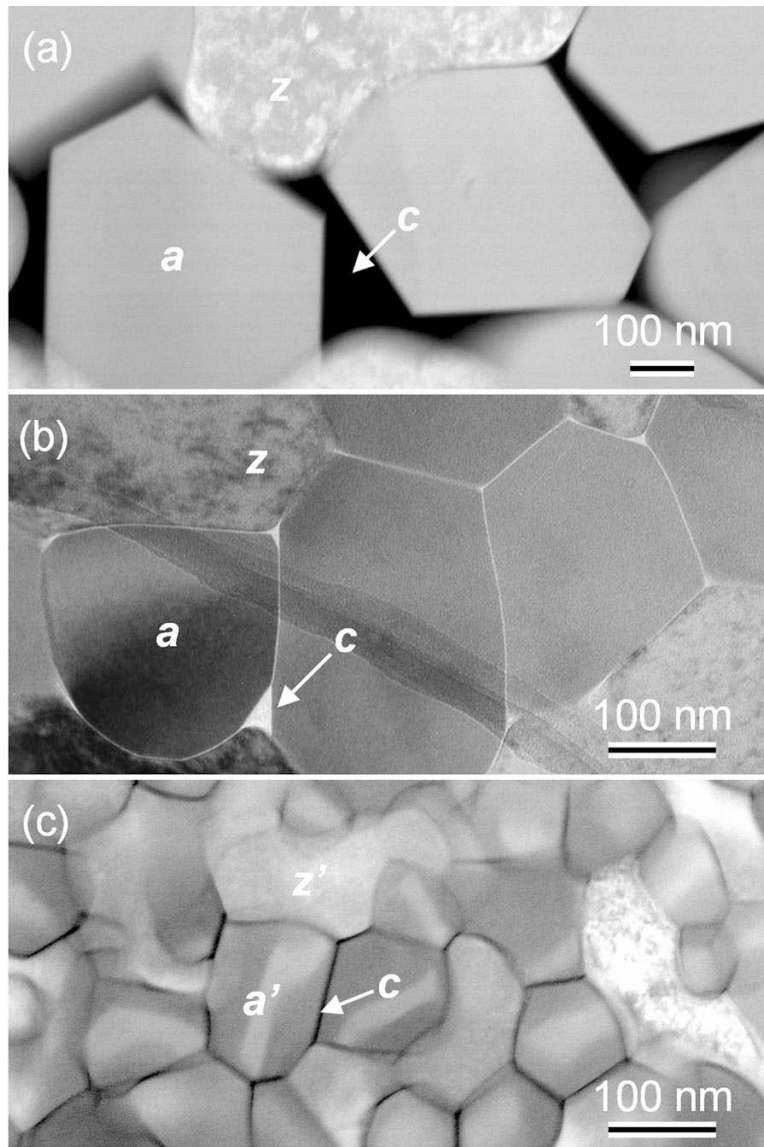


Figure 7: Microstructures of in-plane sections within the reaction zone taken at distances of (a) 5 μm , (b) $\sim 2 \mu\text{m}$, and (c) 800 nm from the GZO interface. (a, c) are recorded in HAADF TEM mode revealing the Z-contrast between crystallites and surrounding CMAS. The BF micrograph in (b) highlights the glassy nature of the grain boundary films. See Table I for chemical compositions.

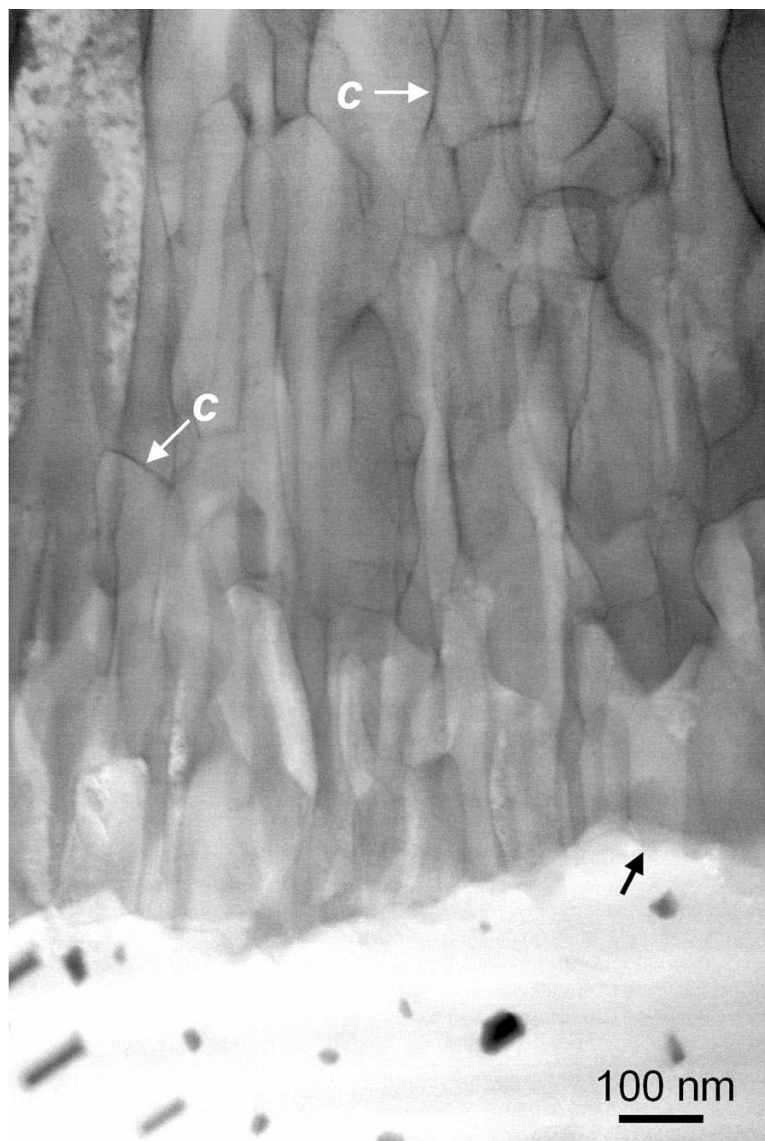


Figure 8: HAADF TEM micrograph of the interface between GZO and the lower part of the reaction zone, from a lamella taken at the position and orientation denoted by D in Fig. 4.

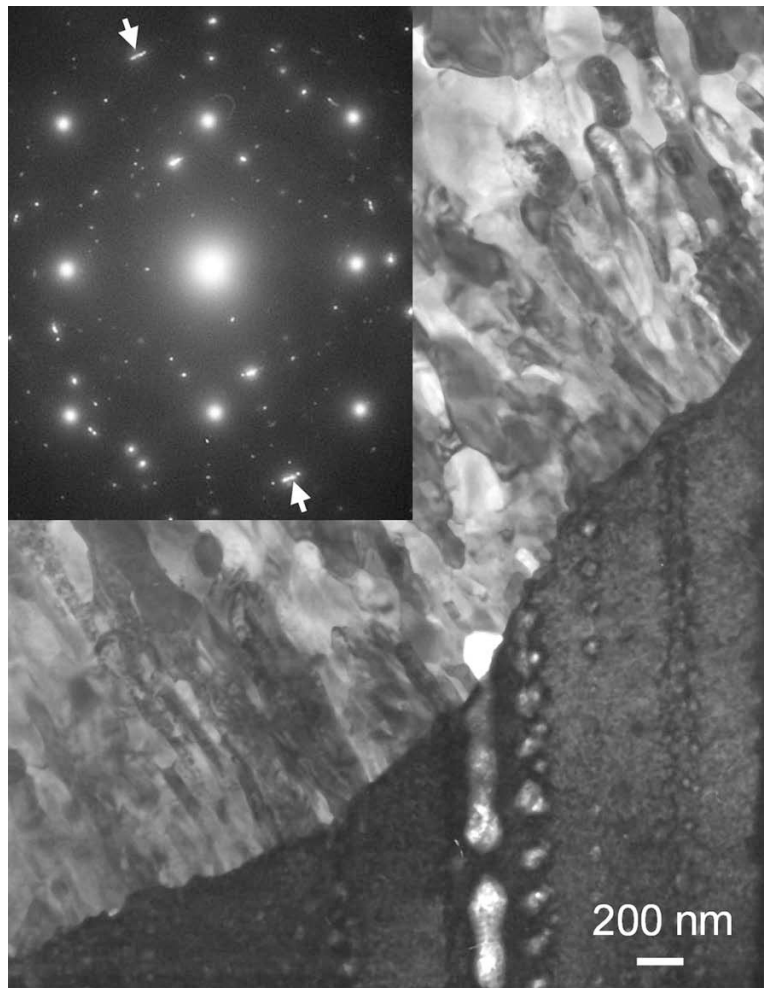


Figure 9: Bright field TEM micrograph of the interface between GZO and the lower part of the reaction zone with the electron beam parallel to the GZO $\langle 100 \rangle$ zone axis. The diffraction pattern (inset) at the interface reveals no special crystallographic relationship between GZO and the adjacent columnar grains of apatite and fluorite products.

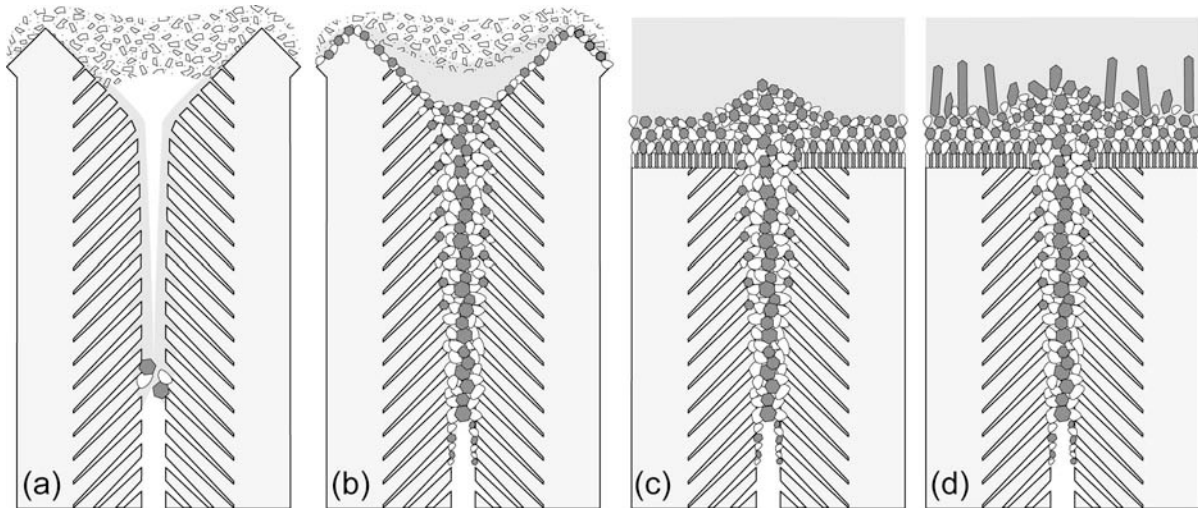


Figure 10: Schematic of the envisaged mechanism leading to the microstructure of the reaction layer. (a) early stages wherein the incipient melt wicks down the column sides, leading to the nucleation of the reaction products within the channel; (b) channel fills up with reaction products hindering further penetration of the melt, while column tips are only moderately attacked at this stage; (c) column tips are gradually attacked by the bulk CMAS melt forming a graded microstructure; (d) additional growth of crystalline phases takes place during cooling.